



Use of Constrained Gamma Emission Computed Tomography to Evaluate Fission Product Distributions in High-Temperature Materials from a TRISO Fuel Irradiation

Changing the World's Energy Future

Adriaan Anthony Riet, John D Stempien



DISCLAIMER

This information was prepared as an account of work sponsored by an agency of the U.S. Government. Neither the U.S. Government nor any agency thereof, nor any of their employees, makes any warranty, expressed or implied, or assumes any legal liability or responsibility for the accuracy, completeness, or usefulness, of any information, apparatus, product, or process disclosed, or represents that its use would not infringe privately owned rights. References herein to any specific commercial product, process, or service by trade name, trade mark, manufacturer, or otherwise, does not necessarily constitute or imply its endorsement, recommendation, or favoring by the U.S. Government or any agency thereof. The views and opinions of authors expressed herein do not necessarily state or reflect those of the U.S. Government or any agency thereof.

Use of Constrained Gamma Emission Computed Tomography to Evaluate Fission Product Distributions in High-Temperature Materials from a TRISO Fuel Irradiation

Adriaan Anthony Riet, John D Stempien

May 2025

**Idaho National Laboratory
Idaho Falls, Idaho 83415**

<http://www.inl.gov>

**Prepared for the
U.S. Department of Energy
Under DOE Idaho Operations Office
Contract DE-AC07-05ID14517**

Use of constrained gamma emission computed tomography to
evaluate fission product distributions in high-temperature
materials from a TRISO fuel irradiation

Adriaan A. Riet,^{*,a} and John D. Stempien^a

*^aIdaho National Laboratory, Fuel Development Performance and Qualification Department
1955 N Fremont Ave, Idaho Falls, ID 83415*

*Email: adriaan.riet@inl.gov

Number of pages: 24
Number of tables: 0
Number of figures: 11

Abstract

An image reconstruction technique was developed to overcome problems with earlier methods of gamma-emission computed tomography of graphite rings surrounding the AGR-3/4 TRISO fission product transport experiment. The profiles obtained from the tomography are compared with sampling done via radially resolved destructive sampling techniques. Generally, there is good agreement between profiles measured via destructive sampling of the rings and the tomographic profiles, though at low signal strengths, the tomographic profiles appear elevated.

Keywords — Gamma Emission Computed Tomography, Reconstruction, AGR, Nuclear Graphites, Fission Products, TRISO, Advanced Gas Reactor (AGR) 3/4 experiment, nuclear-grade graphite, fission-product transport

I. INTRODUCTION

The United States Department of Energy’s Advanced Gas Reactor (AGR) Fuel Development and Qualification Program was established to perform research and development on tristructural isotropic (TRISO)-coated particle fuel to support the development of high-temperature gas-cooled reactors (HTGRs). These experiments are intended to provide data on fuel performance under irradiation, support fuel fabrication process development, qualify fuel for normal and off normal conditions, provide irradiated fuel for accident testing, and support the development of fuel performance and fission transport models [1].

I.A. AGR-3/4

The AGR-3/4 experiment was designed to irradiate fuel containing TRISO-coated driver fuel particles and designed-to-fail (DTF) fuel particles to act as a source of fission products for subsequent transport through compact matrix and structural graphite materials, and to support the refinement of fuel performance and fission transport models [2]. The DTF particles consisted of a fuel kernel composed of a heterogenous mixture of uranium carbide and uranium oxide coated in a highly anisotropic pyrolytic carbon layer that was nominally 20- μm thick. The experiment consisted of 12 capsules [3] irradiated in the northeast flux-trap position of the Advanced Test Reactor at the Idaho National Laboratory (INL) [4]. The capsules consisted of four compacts, each filled with approximately 1,898 TRISO-coated driver particles and exactly 20 DTF particles arranged along the center of the cylindrical compact’s long axis [5]. Four compacts were stacked in the center of each capsule and surrounded by three concentric sleeves (rings) of graphitic matrix or graphite, referred to respectively as inner (IR), outer (OR), and sink rings (SR) (see Figure 1). Gaps between the compacts and the rings allowed for a mixture of helium and neon gas to flow for the purpose of controlling the temperature via in each capsule and for sweeping fission gases to a fission product monitoring system. The experiment lasted for 369.1 effective full power days [6]. Time-dependent thermal profiles for each capsule were generated using a model built in ABAQUS software that was evaluated in comparison to readings from three thermocouples embedded in the capsules [7], and fission product release rates were predicted using JMOCUP and PARFUME software [8, 9].

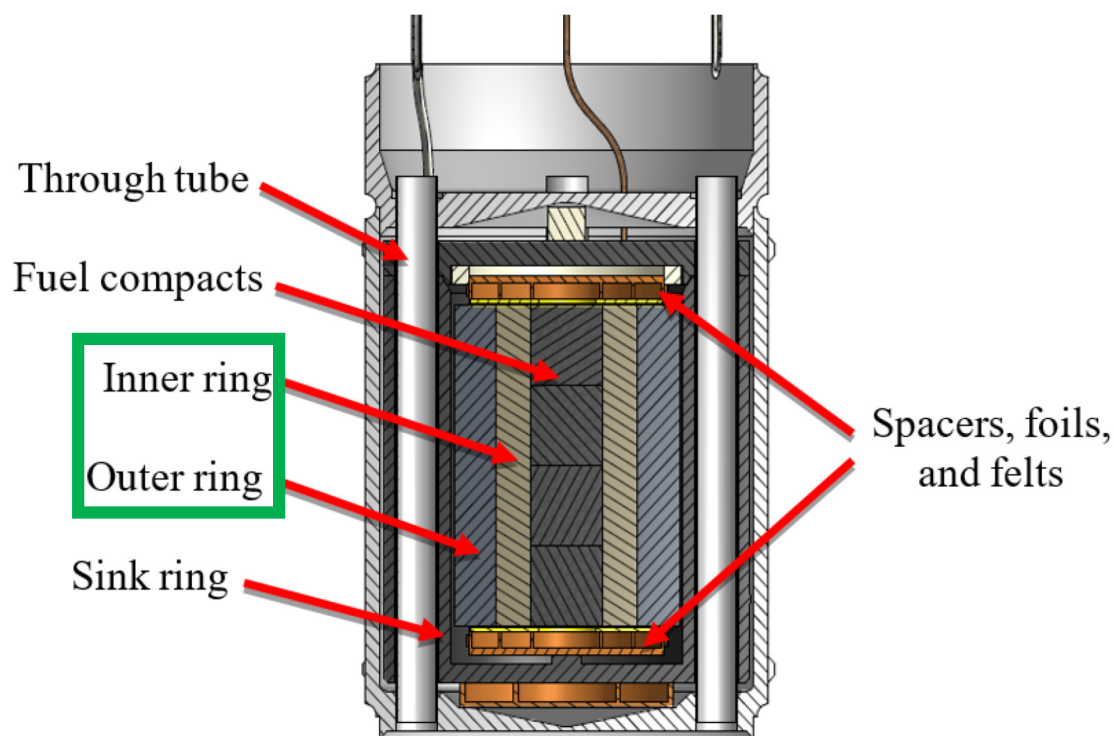


Fig. 1. Cross section of a typical standard capsule. The 20 DTF particles are located in the center of the compacts. Gamma scanning referenced in this work was limited to the IR and OR, labels highlighted in the green box.

I.B. Prior work

After irradiation, the test train was removed and some of the capsules (3, 4, 5, 7, 8, 10, and 12) were dismantled and their inner and outer rings were gamma-scanned using the precision gamma scanner at INL's hot-fuel examination facility. Scans were taken in two different orientations, axial and tomographic. Axial scans were done by scanning down the length of one side of the ring and then using a second set of scans to scan the second side to obtain total fission product inventories and axial distributions, as shown in Figure 2. Though the axial scans were approximately centered on the ring, there may have been some offset such that one scan line covered more of the sample than the other. For "axial" scans, the scanner was oriented for maximal resolution in the axial direction (lengthwise down the cylinder). Tomographic scans were then taken by orienting the collimator to increase the resolution in the radial directions, and repeatedly scanning across, then rotating the sample as shown in Figure 2 [10]. Each scan consisted of gamma-counting for between 30 and

90 minutes, with a total number of scans per axial height of between 75 and 360 resulting in total collection times per axial position between 10 and 230 hours. Gamma-spectroscopic measurements were taken after a decay time of at least twelve months. All measurements were decay-corrected to one day after the end of the AGR-3/4 irradiation.

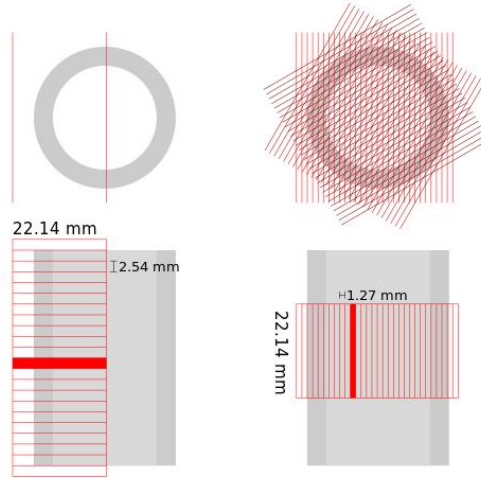


Fig. 2. Scan geometry for axial (left) and tomographic (right) scans of a typical capsule OR. Scans were taken at multiple capsule rotations to generate the tomographic information. Two axial scans were taken 22.2 mm apart and summed to inventory the entirety of the capsule. Though expressed here in metric units, the collimator geometry is defined in inches.

Preliminary reconstructions based on data from the tomographic scans showed some non-physical properties. The reconstruction exhibits non-zero fission product concentrations in regions not occupied by the rings, both radially external to the ring, and in the center of the annulus. When a 2D reconstruction was processed into a 1D circumferentially averaged radial profile (which mimics the collection process used in physical sampling of the rings), this was observed as a smooth gradient of concentration into the area beyond the inner surface of the ring, obscuring the true concentration at the inner surface, and leading to a radial activity profile that has a peak in an incorrect position. In Figure 3, the results of a naïve reconstruction of gamma scans taken at the axial center of the Capsule 3 IR are compared with results from destructive physical sampling [11], which, consistent with several other IR results, demonstrate that these peaks are non-physical. This highlights the need for a more informed method of tomographic reconstruction.

As discussed in Ref. [13], improvements were made to the generic tomographic reconstruction

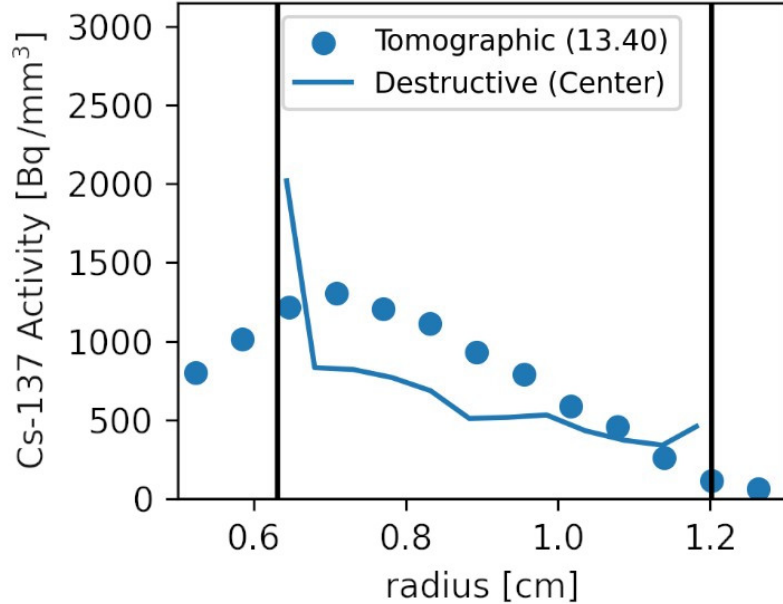


Fig. 3. Naïve reconstruction of radial Cs-137 activity profile from tomographic scans of IR 3 (circles), compared against a destructively measured profile from Ref. [11] (line), with black lines noting the inner and outer radii as measured in post-irradiation examination [12].

algorithm by imposing an annular cylindrical geometry to the reconstructed image. This led to improved agreement with destructive sampling results; although, enforcing a cylindrical system onto the reconstruction requires knowledge of the center of the cylinder, without which the non-physical results are magnified. Furthermore, a Tikhonov regularization parameter [14] was added to enforce smoothness in the reconstruction, but the appropriate value for the Tikhonov regularization parameter was not then explored.

II. METHODOLOGY

Three geometric parameters are important to the reconstruction: the center of the cylinder in the direction perpendicular to the scan axis x_c , and the center of rotation of the cylinder (x_{cr}, y_{cr}) . The measured activity of ^{134}Cs $C_{134\text{Cs}}(x, \phi)$ as a function of scan position was used to obtain an initial estimate of these parameters for a given rotation ϕ via Eq. 1

$$\frac{\sum_x x C_{134\text{Cs}}(x, \phi)}{\sum_x C_{134\text{Cs}}(x, \phi)} = x_{com}(\phi) = x_{com}(0) + (x_c - x_{cr}) \cos(\phi) + y_{cr} \sin(\phi) \quad (1)$$

and best-fit values for x_c , x_{cr} and y_{cr} are found in a least-squares fashion, with the assumption that the center of activity is approximately the same as the center of the cylinder $x_{com}(0) \approx x_c$. The isotope ^{134}Cs was used as it was consistently measured with low error in all of the rings.

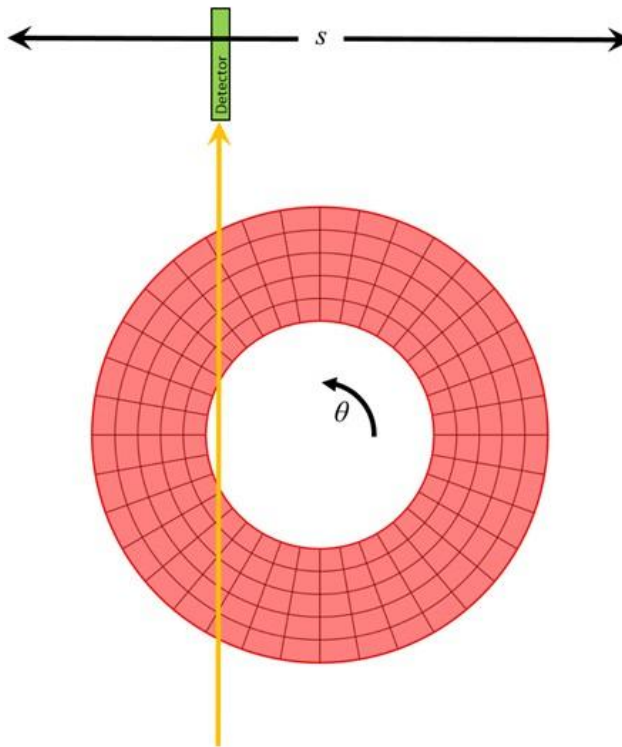


Fig. 4. Reconstruction geometry and pixel map.

With this initial estimate, we then move to a more rigorous centering algorithm. Following Ref. [13], the objective of a reconstruction is to find the pixels of an image f_j such that we can construct from a series of measured activities g_i mapped by a series of viewing windows for each measurement to each pixel M_{ij} , as shown in Eq. 2

$$g_i = \sum_{j=1}^m M_{ij} f_j \quad (2)$$

Beginning with isotopic activities determined from gamma spectral analyses performed via the PCGAP analysis software [15, 16], we generate g_i for each isotope of interest similar to the process used in Ref. [17]. For our basis set of pixels, we use polar elements as depicted in Figure 4, where each element of the polar grid is represented as an element of the vector f_j , and the area of intersections M_{ij} between f_j and the observation window is calculated analytically for all measurements, assuming no diffraction or reflection, so the sample area is a rectangular prism directly in front of the detector. Any measurements with non-zero recorded activity and zero area of intersection are added to the residual (see Section II.A.2).

The scan angles were rounded to the nearest 0.5 degree. We implemented a custom re-

construction algorithm based on the Simultaneous Algebraic Reconstruction Technique (SART), including the above analytical intersection area generation, in C++ using the Eigen 3 library [18] as follows.

II.A. Reconstruction

II.A.1. Modified SART

Beginning with the set of all measured activities from tomographic scans of a given sample at a given height \vec{g} and the inverse of their uncertainties \vec{e} , an image is constructed using Equations 3-7.

$$\vec{p}^i = \frac{\vec{e}}{\left(\prod_{k=0}^N e_k\right)^{\frac{1}{N}}} \cdot (\vec{g} - \vec{M}^T \vec{f}^i) \quad (3)$$

$$\vec{a}^i = \vec{M} \left(\frac{p_k^i}{\sum_j M_{kj} M_{jk}} \right) \cdot r \quad (4)$$

$$\min(\vec{a}^i + \vec{f}^i) >= 0 \begin{cases} \vec{a}^i = \vec{a}^i \\ j = j \in i \mid a_j + f_j = \min(\vec{a}^i + \vec{f}^i), \vec{a}^i = \vec{a}^i \cdot \frac{f_j}{a_j} \end{cases} \quad (5)$$

$$f^{i+1} = \vec{f}^i + \vec{a}^i \quad (6)$$

$$\|p^{i+1}\| > \|p^i\| \begin{cases} r = r/2 \text{ and recalculate} \\ r = \min(1.1r, 1.5) \end{cases} \quad (7)$$

A brief explanation of these equations is in order. The solution is found as an iterative process, with i denoting the index of the current estimate. The weighted errors are used to calculate the misfit \vec{p}^i between the vector corresponding to the pixels of the image \vec{f}^i and the vector of gamma scans \vec{g} . In Eq. 4, an adjustment vector \vec{a}^i is calculated by mapping the misfit \vec{p}^i to the image space through the viewing matrix M , while normalizing each misfit index k by the magnitude of the viewing matrix for that location. The scalar r is merely a scaling factor used to facilitate faster convergence. If a potential adjustment \vec{a}^i would cause the image vector \vec{f}^i to have negative elements, \vec{a}^i is scaled such that the smallest magnitude in the image vector f^{i+1} will be zero through Eq. 5. After applying the adjustment vector to the current image, the magnitude of the misfit is recalculated to ensure that the error has been reduced through Eq. 7. If not, the iteration is recalculated with a smaller scaling factor r . This process is iterated until $\|p^{i+1}\|$ is less

than 10^{-16} or stops decreasing.

This algorithm is similar to the traditional SART algorithm [19], but with a few differences. First, the area of intersection is calculated analytically. Second, as the standard assumption of convex density centered on the image is not valid, the standard weighting applied (Hamming window) is inappropriate, so the weighting is replaced by an uncertainty-based weighting scheme. Third, instead of grouping by sets of measurements at different scan angles, every measurement is included in each image refinement step. Attenuation of gamma rays in the graphite was considered to be negligible given the small size of the sample, and was neglected in the reconstruction process.

II.A.2. Centering

A best-estimate of center was calculated using the nmsimplex2 algorithm of the GNU Scientific Library [20] with an objective function that summed the specific error associated with the reconstruction after convergence p and all unaccounted for measurements. “Unaccounted for” measurements are measurements of activity in scans that do not intersect the reconstructed image at any point. These were weighted by the total volume of the measured ring, e.g. for unaccounted activity C and ring volume V the objective function $J(x_c, x_{cr}, y_{cr})$ is defined in Eq. 8

$$J(x_c, x_{cr}, y_{cr}) = \sum_{isotopes} \|p_{isotope}^{final}\| + C_{isotope}V \quad (8)$$

, which applied a large penalty to any unaccounted for measurements. Only isotopes with small measurement errors in a majority of scans (^{134}Cs , ^{137}Cs and ^{60}Co) were used in the centering algorithm.

II.A.3. PaPIRuS

In comparison with PaPIRuS, the algorithm above has good computational efficiency and a smoother objective function when used to find the cylinder location and center of rotation, but was less accurate at accounting for sudden changes in concentration recorded in destructive physical sampling measurements [21]. As noted previously, the PaPIRuS algorithm requires a Tikhonov regularization parameter λ to dampen spurious assignment of concentration throughout the reconstruction, sometimes referred to as “salt and pepper” noise, which can occur because there can be more than one mathematically consistent solution. The activity concentration on the

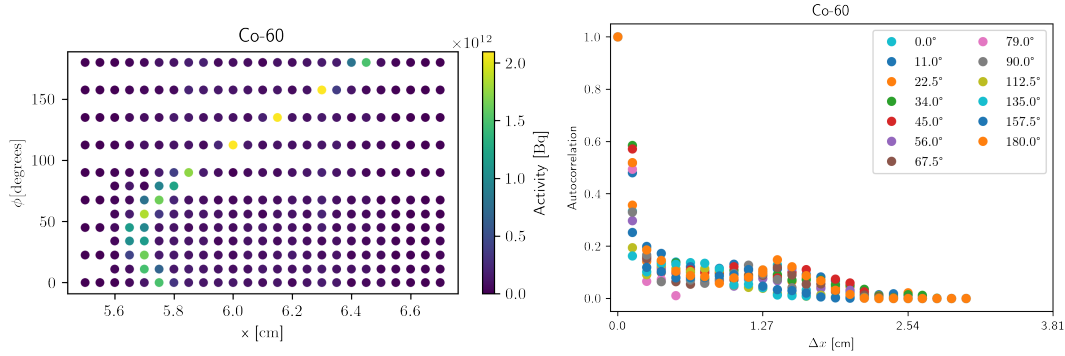


Fig. 5. Left: ^{60}Co activity in IR 3 as a function of detector position and scan angle in degrees. Right: Autocorrelation of activity as a function of detector position, individually plotted for each scan angle

polar grid is then obtained using Eq. 9

$$\|Mf - g\|_2^2 + \sqrt{\lambda^2 \sum_{j=2}^{m-1} (f_{j-1} - 2f_j + f_{j+1})^2} \quad (9)$$

As can be seen, λ penalizes oscillatory solutions. From the perspective of a simple theoretical model of the AGR-3/4 experiments (designed as 1-D radial diffusion experiments) this should be a non-issue because significant oscillations were not expected; however, to avoid masking real oscillatory behavior, a value of λ was chosen that did not mask local phenomena. In Capsule 3, a melt wire alloy composed of 70/30% Cu/Ni was inserted into a hole in the mid-plane of the ring. Because of neutron activation of the melt wire, we observe a strong, localized signal of ^{60}Co , as shown in the sinogram and autocorrelation functions from a set of tomographic scans near the center of the IR in Fig. 5. There is also the potential for diffuse ^{60}Co in the sample from neutron activation of trace contamination in the graphite, which was analyzed for PCEA samples by EAG laboratories using glow-discharge-mass-spectrometric analysis. Specific impurities in the sampled PCEA relevant to ^{60}Co generation were found to be Fe 0.06, Co <0.05, and Ni <0.1 parts per million by weight. Thus the majority of the ^{60}Co is from the activation of the melt wire. The localization of the signal in real measurements can be observed in the immediate decline of the autocorrelation function.

A Tikhonov regularization parameter was selected by comparison of tomographic reconstructions, selecting for a parameter that minimized noise without substantially affecting localized phenomena, as shown in Fig. 6.

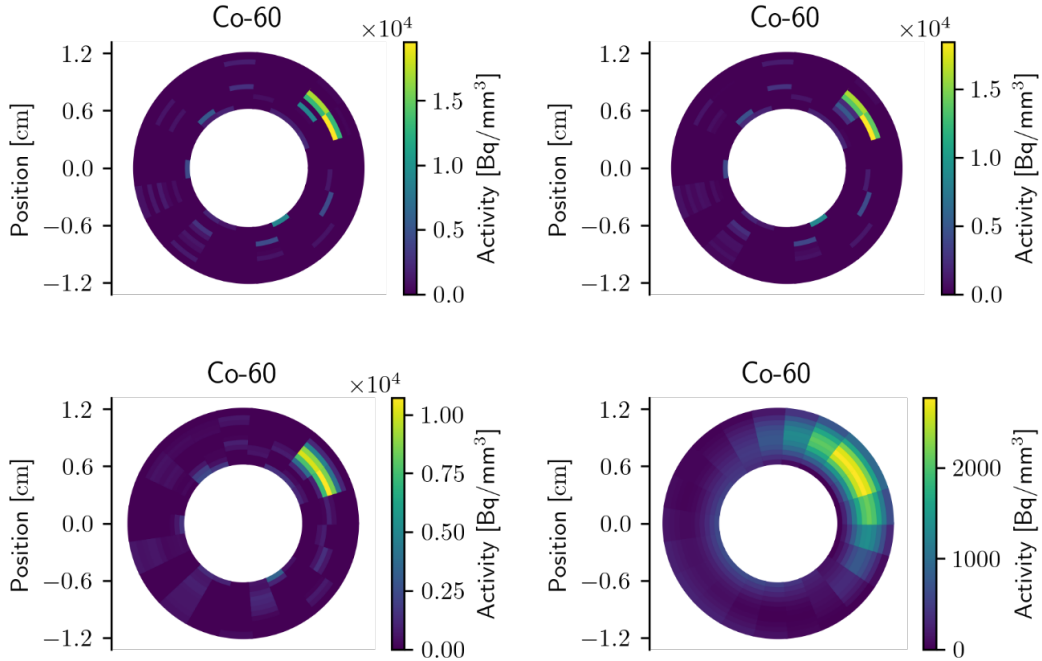


Fig. 6. Reconstructions of the tomographic scans of IR 3 in Fig. 5 with different Tikhonov regularization parameters. Top left, $\lambda = 0.0005$. Top right, $\lambda = 0.005$. Bottom left, $\lambda = 0.03$. Bottom right, $\lambda = 0.5$.

Low values of λ do not constrain the observed local activity, but also do not constrain spurious activity. Large values of λ smear the local activity across several contiguous elements and do not accurately reflect the maximum concentration, a pivotal factor in understanding whether transport is surface-limited. We determined by visual inspection of the ^{60}Co concentration profiles that $\lambda = 0.03$ was sufficient to minimize recorded spurious activity without compromising the integrity of the reconstruction with respect to local phenomena and with minimal effect on the observed peak concentration. This value was then universally applied for all isotopes and all reconstructions, including those shown in Figs. 7-11. A more rigorous sensitivity analysis was not applied.

III. RESULTS AND DISCUSSION

We compare a selection of measurements obtained by destructive sampling (using gamma counts of samples obtained by radial sectioning of the rings) as found by Stempien [11] with those obtained via tomographic scanning. Measurements for other capsules are available in a public

report [21]. The axial length of the radial sections taken was 10.0 mm (approximately 0.394 inches), which is smaller than the 0.875 inches (2.22 cm) axial length sampled in the tomographic scans. Because of this, the actual concentration of areas sampled at the same nominal position may differ. The general organization of Fig. 7-9 is as follows: On the left is an activity heatmap generated using the PaPIRuS tomographic reconstruction algorithm detailed in Section II.A.3 on the scanning data with the center-of-cylinder determined using the modified SART algorithm described in Section II.A.1-II.A.2. On the right, the radial concentration profiles determined in Ref. [11] are compared with the radial concentration profile obtained by taking radial averages of the computed concentrations (circles and ‘+’ signs). Using Hawkes’ thermal analysis [7] for the time-average temperatures of the inside and outside of the rings, the time-average temperature profile is reproduced as a dashed line on the right for use as a reference.

III.A. IR 3

As can be seen by Fig. 7, concentrations within the radial profiles of activities obtained from tomographic reconstruction tended to be higher than those from destructive analysis. Additionally, it can be seen that large $^{110\text{m}}\text{Ag}$ activity located in the annular midplane observed in the destructive analysis is localized to a high-activity region on one side of the cylinder. Cesium and silver are both mobile in the graphite, while europium exhibits primarily slow transport. Though at low concentrations (approximately 10-100 Bq/mm³ or $10^9 - 10^{10}$ atoms/mm³), the radial concentration profile of europium suggests that limited amounts of europium transport more rapidly than the experiment can resolve may also be occurring in low-capacity transport channels such as grain boundary or triple-junction facilitated diffusion.

III.B. IR 4

In IR 4, the radial concentration profiles of ^{134}Cs and ^{137}Cs are similar to each other. Both tomographic and destructive testing show a local concentration maximum within the ring, as shown in Fig. 8. The tomographic reconstructions indicate a much larger concentration of Cs isotopes at the inner surface of the ring than the measurements obtained by destructive sampling. For $^{110\text{m}}\text{Ag}$, however, destructive sampling indicates elevated concentrations relative to those obtained via tomographic reconstruction. There is larger disagreement between the tomographic and destructive

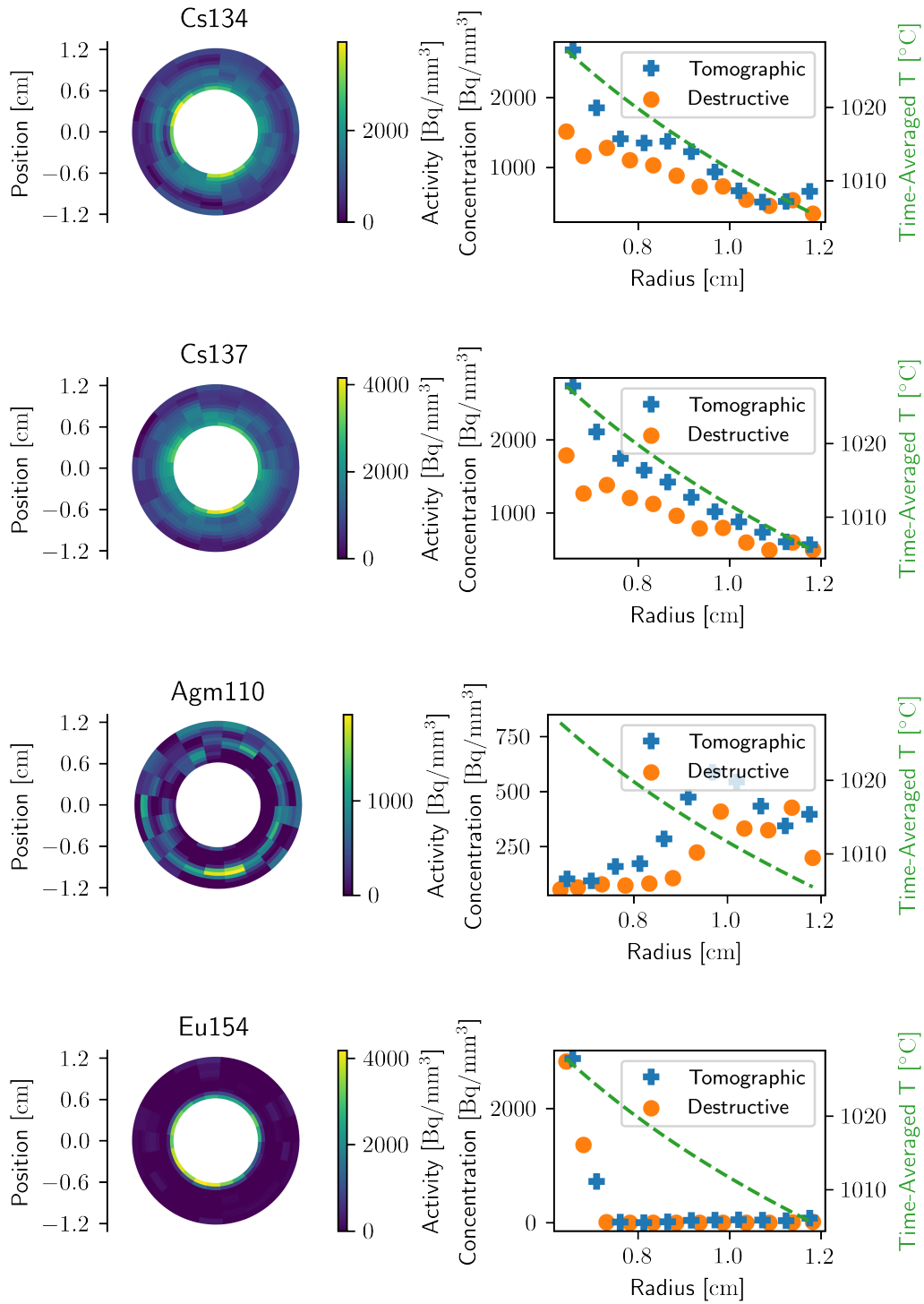


Fig. 7. Activity profiles measured near the center of IR 3, along with activity heatmaps from tomographic reconstruction and radial profiles from destructive physical analysis.

sampling for ^{154}Eu , though this is likely due to insufficient scan time to resolve ^{154}Eu concentrations in the tomographic scanning based on concentrations observed in destructive analysis, as longer scan times would lower the minimum detectable activity (MDA) limit. An analysis with extended scan times is likely not practically feasible as the scan times become quite large.

III.C. IR 7

For IR 7, the tomographic reconstructions again show an increase in Cs inside the ring, though there is a discrepancy between the location of the peak activities observed for ^{134}Cs and ^{137}Cs , see Fig. 9. Additionally, there were no tomographic scans in IR 7 that resulted in a $^{110\text{m}}\text{Ag}$ activity above the minimum detectable limit (MDL). The penalization of large discontinuities in the tomographic reconstruction enforced by λ at the 0.03 level leads to over-smoothing for ^{154}Eu , as only two radial locations account for the majority of the concentration profile. To allow for this, in Fig. 9, we show ^{154}Eu reconstruction with a $\lambda = 0.0001$. With this adjustment, there is good agreement between the tomographic reconstruction and destructive radial profiling for ^{154}Eu .

III.D. OR 3

Tomography of the ORs required many more scans and much longer total scan times, as there was a much larger total scan volume, and the activities were generally lower than for IR scans. In OR 3, only three scans showed above-MDL activities for $^{110\text{m}}\text{Ag}$, and no above-MDL activity was observed for ^{154}Eu . For isotopes of Cs, a significant number of scans did not detect Cs. For ^{134}Cs and ^{137}Cs , only 17% and 62% of scans recorded above-MDL activities, with peak recorded activities 2.2 and 5.9 times the average MDL, respectively. As such, only Cs isotopes are shown in Fig. 10, the other isotopes having insufficient data to generate a valid reconstruction. Perhaps interestingly, there are observed local maxima in the tomographic reconstructions at both the inner and outer surfaces and at a midpoint radius of the ring. The magnitude of this effect may be an artifact of the reconstructions, but the effect is observed using both destructive and tomographic analysis.

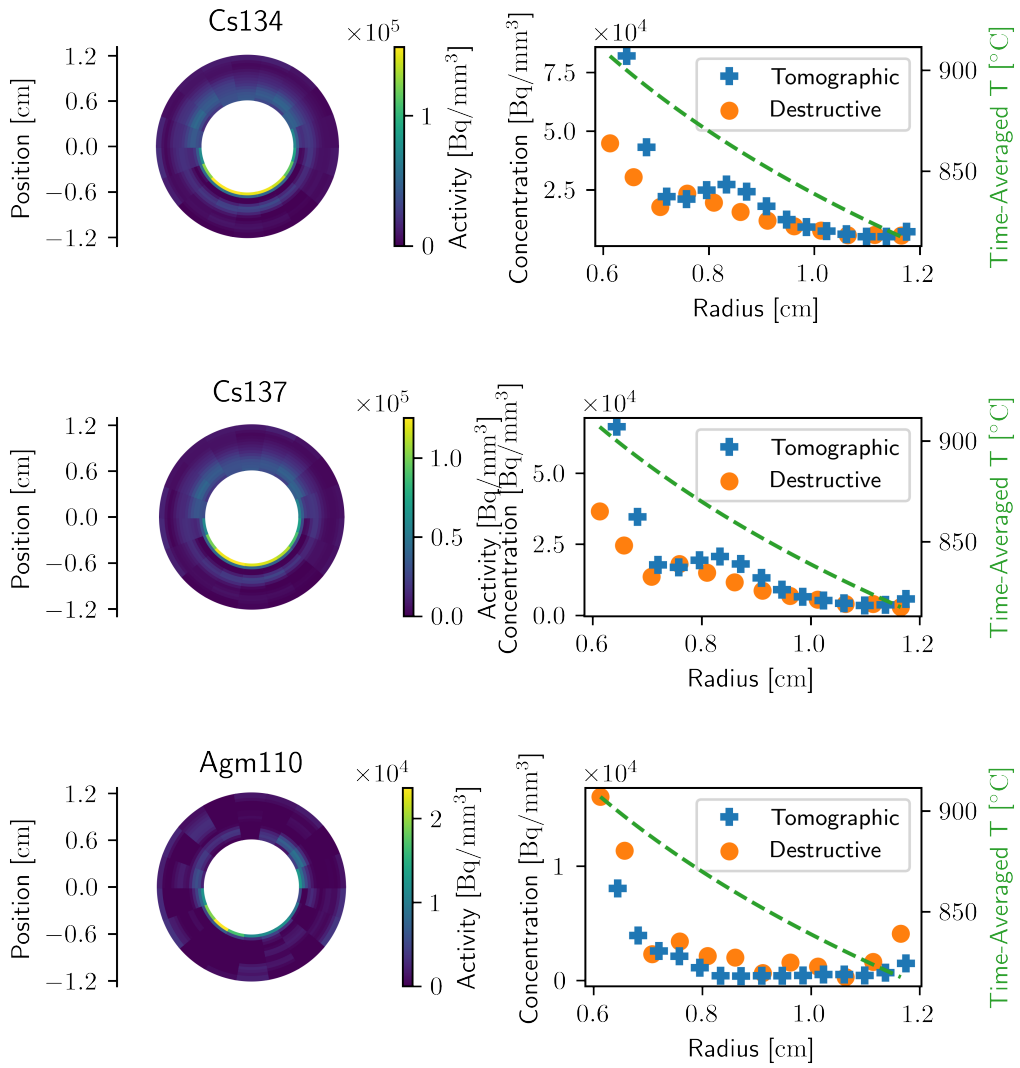


Fig. 8. Activity profiles measured near the center of IR 4, along with activity heatmaps from tomographic reconstruction and radial profile from destructive physical analysis.

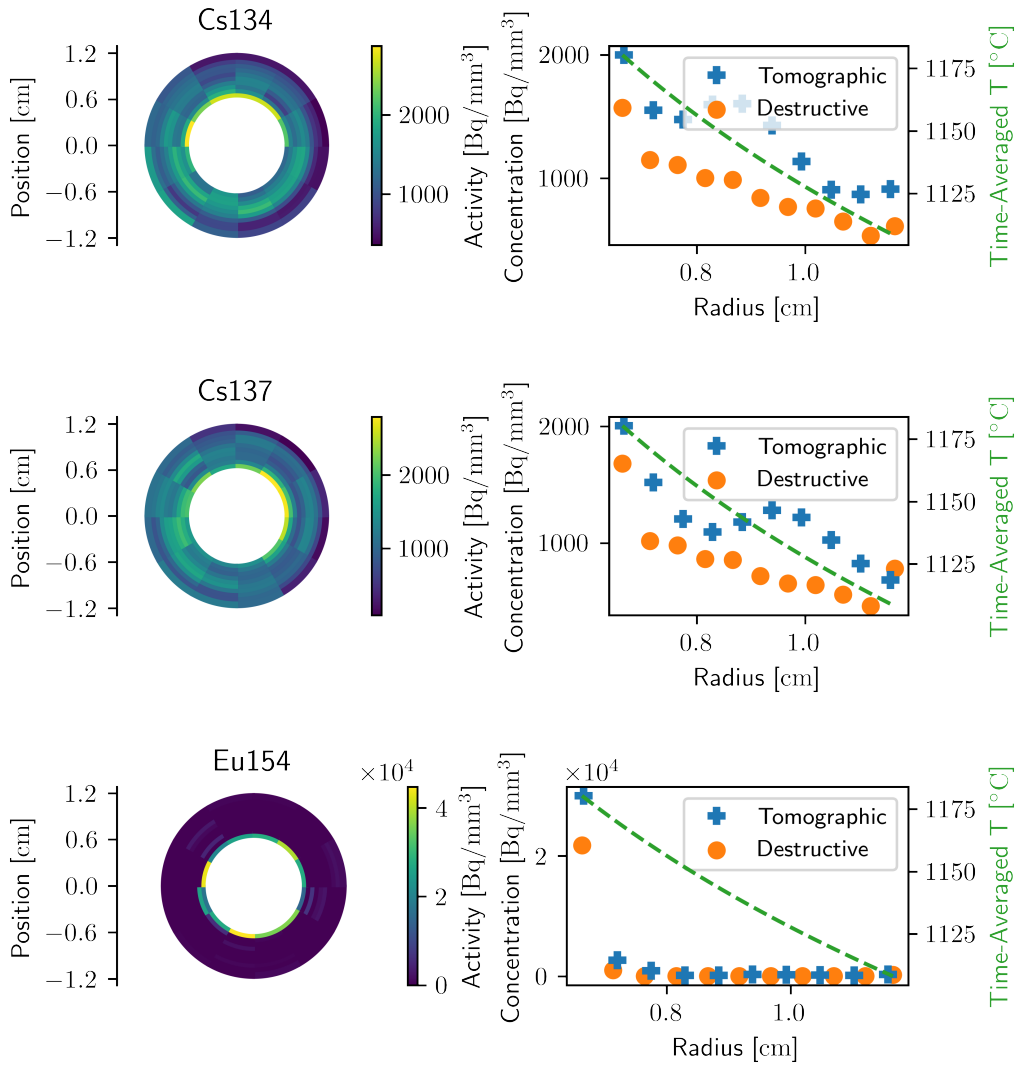


Fig. 9. Activity profiles measured near the center of IR 7, along with activity heatmaps from tomographic reconstruction and radial profile from destructive physical analysis. The ^{154}Eu data is computed with $\lambda = 0.0001$ to avoid artifacts due to the short concentration gradient.

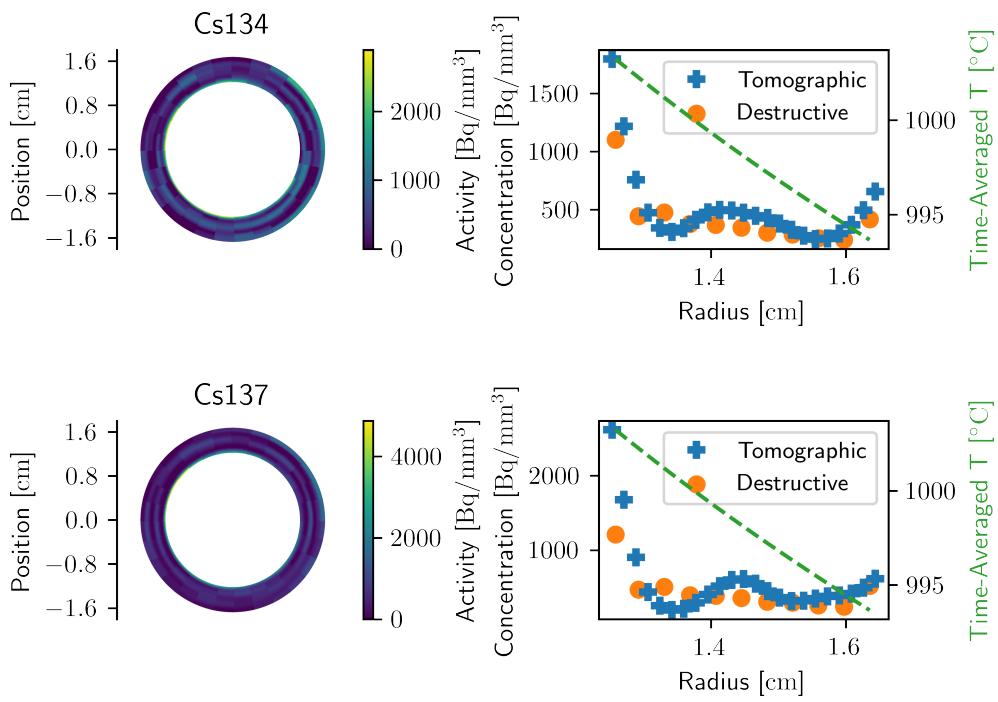


Fig. 10. Activity profiles measured near the center of OR 3, along with activity heatmaps from tomographic reconstruction and radial profile from destructive physical analysis.

III.E. OR 8

Within OR 8, the tomographic reconstructions followed the form of the destructive analyses, though the magnitude of the recorded activity was inconsistent. Tomographic scanning yielded 80-90% above-MDL activity for ^{134}Cs , ^{137}Cs and $^{110\text{m}}\text{Ag}$, with peak signal strength between 17-40 times the average MDL. There remains some uncertainty about the appropriate level of smoothing, though it is clear from the form of the Cs reconstructions that the local maxima of concentrations in the middle of the radial concentration profiles are documenting real phenomena. The radial concentration profile of $^{110\text{m}}\text{Ag}$ is the most inconsistent, with the concentrations of the inner section showing the worst agreement. As the radial concentration profile is an average, and errors in the tomographic reconstruction would skew towards over-estimation of low-recorded concentrations, this may be an artifact due to the large angular variation in $^{110\text{m}}\text{Ag}$ activity. It is clear from both the destructive analysis and the tomographic reconstructions in Fig. 11 that the concentration profiles in OR 8 are more complicated than would be expected from 1-D radially symmetric isotropic diffusion. The non-symmetrical nature of the concentration profiles in OR 8 may be related to variations with the DTF particle distribution, which may be offset by a few millimeters from the compact centerline [5], or the asymmetry may be due to thermal gradients caused by the rings or compact being offset from the center of the capsule, which has been found in another experiment, though this has not yet been investigated for AGR 3/4 [22, 23].

IV. CONCLUSIONS

We demonstrated a novel geometrically-constrained tomographic reconstruction technique, and used it to map fission product concentrations in nuclear-grade graphites and matrix media used in the AGR-3/4 TRISO fuel irradiation experiment. We observed agreement between destructive analysis and tomographic reconstructions, with the additional capacity to resolve angular variation in concentration profiles. The drawbacks of the method are primarily related to the attenuation of the signal within the PGS system, resulting in long collection times and limiting the total number of scans which could be performed. Cesium showed primarily uniform radial concentration profiles, while $^{110\text{m}}\text{Ag}$ had significant angular variations in concentration. Europium transport was limited, and there was good agreement between the destructive and tomographic analysis techniques. With the possible exception of $^{110\text{m}}\text{Ag}$, these tomographic reconstructions provide evidence supporting

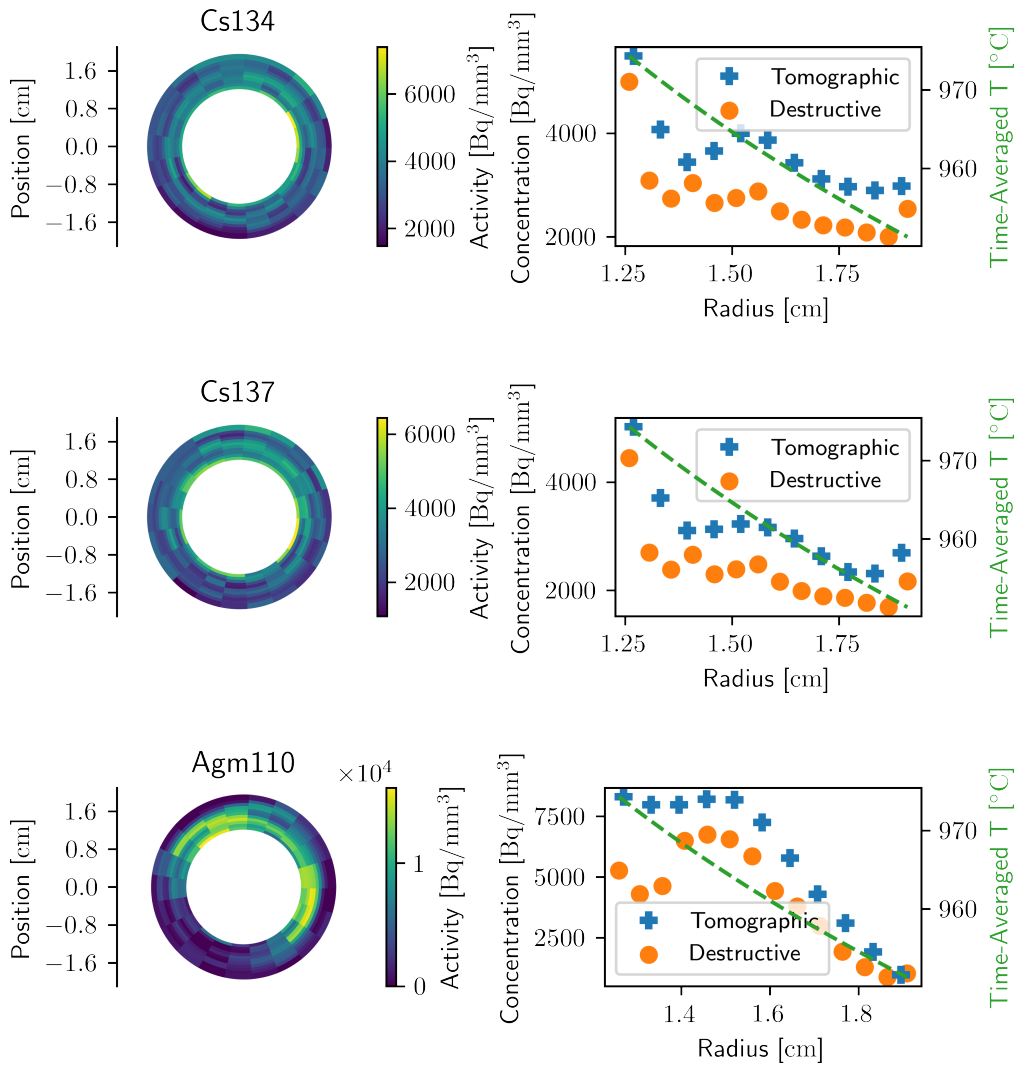


Fig. 11. Activity profiles measured near the center of OR 8, along with activity heatmaps from tomographic reconstruction and radial profile from destructive physical analysis.

the assumption that there is not an angular dependence on fission product transport. Models of fission product transport over the course of the AGR 3/4 experiment will be compared to these results in future work.

ACKNOWLEDGMENTS

This work was sponsored by US DOE Office of Nuclear energy, and was completed under contract number DE-AC07-05ID14517. The authors would like to thank Paul Humrickhouse for his valuable contributions to the present work.

REFERENCES

- [1] T. R. MITCHELL and P. A. DEMKOWICZ, “Technical Program Plan for INL Advanced Reactor Technologies; Technology Development Office / Advanced Gas Reactor Fuel Development and Qualification Program,” PLN-3636, Idaho National Laboratory (2020).
- [2] B. P. COLLIN, “AGR-3/4 Irradiation Experiment Test Plan,” INL/MIS-11-22351, Idaho National Laboratory (2015).
- [3] J. D. HUNN, R. A. LOWDEN, J. H. MILLER, B. C. JOLLY, M. P. TRAMMELL, A. K. KERCHER, F. C. MONTGOMERY, and C. M. SILVA, “Fabrication and characterization of driver-fuel particles, designed-to-fail fuel particles, and fuel compacts for the US AGR-3/4 irradiation test,” *Nuclear Engineering and Design*, **271**, 123 (2014); 10.1016/j.nucengdes.2013.11.020.
- [4] B. P. COLLIN, P. A. DEMKOWICZ, D. A. PETTI, G. L. HAWKES, J. PALMER, B. T. PHAM, D. M. SCATES, and J. W. STERBENTZ, “The AGR-3/4 fission product transport irradiation experiment,” *Nuclear Engineering and Design*, **327**, 212 (2018); 10.1016/j.nucengdes.2017.12.016., URL <https://doi.org/10.1016/j.nucengdes.2017.12.016>.
- [5] J. D. HUNN, M. P. TRAMMELL, and F. C. MONTGOMERY, “Data Compilation for AGR-3/4 Designed-To-Fail (DTF) Fuel Compact Lot (LEU03-10T-OP2/LEU03-07DTF-OP1)-Z,” *Oak Ridge National Laboratory*, ORNL/TM-2011/124 (2011).
- [6] B. P. COLLIN, “AGR-3/4 Irradiation Test Final As-Run Report,” INL/EXT-15-35550, Idaho National Laboratory (2015) URL <https://inldigitallibrary.inl.gov/sites/sti/sti/6305200.pdf>.
- [7] G. L. HAWKES, “AGR-3/4 Daily As-Run Thermal Analyses,” ECAR-2807, Idaho National Laboratory (2016).
- [8] J. W. STERBENTZ, “JMOCUP As-Run Daily Physics Depletion Calculation for the AGR-3/4 TRISO Particle Experiment in ATR Northeast Flux Trap,” ECAR 2753, Idaho National Laboratory (2015).

- [9] W. F. SKERJANC, “AGR-3/4 Irradiation Test Predictions using PARFUME,” INL/EXT-16-38280, Idaho National Laboratory (2016).
- [10] J. M. HARP, P. A. DEMKOWICZ, and J. D. STEMPIEN, “Initial Gamma Spectrometry Examination of the AGR-3/4 Irradiation,” *International Topical Meeting on High Temperature Reactor Technology, Las Vegas*, INL/CON-16-39738, HTR (2016) URL <https://www.osti.gov/biblio/1358395>.
- [11] J. D. STEMPIEN, “Measurement of fission product concentration profiles in AGR-3/4 TRISO fuel graphitic matrix and nuclear graphites,” INL/EXT-21-62863, Idaho National Laboratory (2021).
- [12] J. D. STEMPIEN, F. J. RICE, P. L. WINSTON, and J. M. HARP, “AGR-3/4 Irradiation Test Train Disassembly and Component Metrology First Look Report,” INL/EXT-16-38005, Idaho National Laboratory (2016).
- [13] P. W. HUMRICKHOUSE, J. D. STEMPIEN, J. M. HARP, P. A. DEMKOWICZ, and D. A. PETTI, “Preliminary Estimation of Fission Product Diffusion Coefficients from AGR-3/4 Data,” *Proceedings of HTR 2018* (2018).
- [14] D. CALVETTI, S. MORIGI, L. REICHEL, and F. SGALLARI, “Tikhonov regularization and the L-curve for large discrete ill-posed problems,” *Journal of Computational and Applied Mathematics*, **123**, 1, 423 (2000); [https://doi.org/10.1016/S0377-0427\(00\)00414-3](https://doi.org/10.1016/S0377-0427(00)00414-3), URL <https://www.sciencedirect.com/science/article/pii/S0377042700004143>, numerical Analysis 2000. Vol. III: Linear Algebra.
- [15] E. W. KILLIAN and L. V. EAST, “PCGAP: Application to analyze gamma-ray pulse-height spectra on a personal computer under Windows NT[®],” *Journal of Radioanalytical and Nuclear Chemistry*, **233**, 1, 109 (1998); 10.1007/BF02389656., URL <https://doi.org/10.1007/BF02389656>.
- [16] E. W. KILLIAN and J. K. HARTWELL, “PCGAP: Users Guide and Algorithm Description,” INEEL/EXT-2000-00908, Idaho National Engineering and Environmental Laboratory (2000).

- [17] J. M. HARP, “Analysis of Individual Compact Fission Product Inventory and Burnup for the AGR-1 TRISO Experiment Using Gamma Spectroscopy,” INL/MIS-11-23314-Revision-3, Idaho National Laboratory (2010).
- [18] G. GUENNEBAUD, B. JACOB ET AL., “Eigen v3,” (2010) URL <http://eigen.tuxfamily.org>.
- [19] A. H. ANDERSEN and A. C. KAK, “Simultaneous Algebraic Reconstruction Technique (SART): A Superior Implementation of the ART Algorithm,” *Ultrasonic Imaging*, **6**, 81 (1984).
- [20] M. GALASSI, J. DAVIES, J. THEILER, B. GOUGH, G. JUNGMAN, P. ALKEN, M. BOOTH, F. ROSSI, and R. ULERICH, *GNU Scientific Library Reference Manual Revision 2.7*, Free Software Foundation (2021) URL <https://www.gnu.org/software/gsl/>.
- [21] A. A. RIET, “Reconstruction of Fission Product Distribution from Tomographic Scans in TRISO Fuel Graphitic Matrix and Nuclear Grade Graphites,” INL/RPT-22-67635, Idaho National Laboratory (2022).
- [22] G. HAWKES, B. PHAM, and C. OTANI, “Thermal Model of the AGR-5/6/7 Experiment with Offset Gas Gaps,” *Nuclear Science and Engineering*, 1–26 (2024); 10.1080/00295639.2024.2368994., URL <https://doi.org/10.1080/00295639.2024.2368994>.
- [23] G. L. HAWKES, J. W. STERBENTZ, J. T. MAKI, and B. T. PHAM, “Thermal Predictions of the AGR-3/4 Experiment With Post Irradiation Examination Measured Time-Varying Gas Gaps,” *Journal of Nuclear Engineering and Radiation Science*, **3**, 4, 041007 (2017); 10.1115/1.4037095., URL <https://doi.org/10.1115/1.4037095>.